crystals

MDPI

Article

Ce-Doped Iron Oxide Anticorrosive Coatings: Effect of $c(Ce^{4+}):c(Fe^{3+})$ Ratio on Structure, Morphology, and Coating Anticorrosion Performance

Junxiang Ning [1,*], Xinyi Tang [1] and Peiyang Shi [2]

[1] Academy of Fine Arts, Dalian Art College, Dalian 116600, China; tangxinyi@dac.edu.cn
[2] Key Laboratory for Ecological Metallurgy of Multimetallic Ores (Ministry of Education), School of Metallurgy, Northeastern University, Shenyang 110819, China; shipy@smm.neu.edu.cn
* Correspondence: ningjunxiang@dac.edu.cn

Abstract: Utilizing hydrothermal methods, Ce-doped iron oxide nanoparticles were synthesized from precursor solutions under different $c(Ce^4{:}c(Fe^{3+})$ precursor solutions. The effects of the $c(Ce^{4+}):c(Fe^{3+})$ ratio in the precursor solutions on the nanoparticle morphology and nanoparticle structure of the Ce-doped iron oxide were investigated using X-Ray diffraction, transmission electron microscopy, and scanning electron microscopy. Fourier transform infrared spectroscopy (FTIR) was used to examine the bond energy strength of the Ce-doped iron oxide nanoparticles. The electrochemical properties of the Ce-doped iron oxide nanoparticles were tested using an electrochemical workstation and a saltwater immersion resistance test. The corrosion resistance of Ce-doped iron oxide coatings at different $c(Ce^{4+}):c(Fe^{3+})$ ratios was systematically analyzed, uncovering corrosion resistance mechanisms and self-healing capabilities. The results show that as the $c(Ce^{4+}):c(Fe^{3+})$ ratio decreases, the lattice constants of the samples increase along with the average grain size. Both smaller and larger $c(Ce^{4+}):c(Fe^{3+})$ ratios are detrimental to lattice distortion in α-Fe_2O_3. The reduced number of valence electrons provided by cerium ions in Ce-doped iron oxide hinders the generation of holes and exerts a minor influence on the crystal band structure, leading to weaker electrochemical stability. The Ce-doped iron oxide coating prepared at a $c(Ce^{4+}):c(Fe^{3+})$ ratio of 1:60 readily generates a higher number of reactive hydroxyl radicals during corrosion, thus exhibiting enhanced self-healing capabilities and corrosion resistance.

Keywords: Ce-doped α-Fe_2O_3; coating structure; corrosion resistance; anticorrosive coating

check for updates

Citation: Ning, J.; Tang, X.; Shi, P. Ce-Doped Iron Oxide Anticorrosive Coatings: Effect of $c(Ce^{4+}):c(Fe^{3+})$ Ratio on Structure, Morphology, and Coating Anticorrosion Performance. *Crystals* **2024**, *14*, 923. https://doi.org/10.3390/cryst14110923

Academic Editor: George D. Verros

Received: 26 September 2024
Revised: 20 October 2024
Accepted: 25 October 2024
Published: 26 October 2024

Copyright: © 2024 by the authors. Licensee MDPI, Basel, Switzerland. This article is an open access article distributed under the terms and conditions of the Creative Commons Attribution (CC BY) license (https://creativecommons.org/licenses/by/4.0/).

1. Introduction

Amidst the swift progression of modern industrialization, the need for materials that exhibit superior corrosion resistance has escalated, especially in critical sectors like maritime, chemical, and aerospace applications [1–3]. In these fields, coating materials play a pivotal role in safeguarding the underlying substrates against corrosion, thereby profoundly impacting the safety and longevity of equipment. Ferric oxide (Fe_2O_3), an environmentally benign and readily available nanomaterial, has shown great promise in the coatings sector due to its distinctive physicochemical attributes [4–6]. Nonetheless, the current level of corrosion resistance exhibited by Fe_2O_3 coatings both domestically and abroad significantly lags behind expectations, particularly under severe conditions where their performance deficiencies are acutely highlighted [6–10]. As a result, the pursuit of innovative, modified ferric-oxide coating materials that can markedly enhance corrosion resistance has come to the fore of materials science research.

Iron oxide coatings are used in a wide range of industries such as shipping, power utilities, and automotive industries because of their strong coverage, vibrant colors, and excellent chemical stability. Nevertheless, conventional iron oxide coatings are prone to penetration by corrosive ions when in prolonged contact with electrolytes, leading

to electrochemical corrosion that impairs their stability and corrosion resistance [11–13]. Moreover, these coatings lack an effective passivation mechanism to inhibit corrosion, precluding autonomous repair upon damage and severely limiting their potential application in broader domains [14–16]. Takami et al. [17] used organic surface modifiers ($C_9H_{19}COOH$ and $C_{10}H_{21}NH_2$) for surface modification of iron oxide nanoparticles and found that an organic layer can be formed on the surface of metal oxides, which has the effect of improving the surface physicochemical properties of iron oxide nanoparticles. Bagheri et al. [18] showed that the electromagnetic effect in magnetic nanoparticles is based on electron transfer between Fe^{2+} and Fe^{3+} ions at octahedral positions. Surface modification of magnetic nanoparticles using silica and carbon or surfactants and polymers resulted in the lowering of the number of hydroxyl radicals on the surface of the magnetic nanoparticles, which in turn changed the physicochemical properties of the magnetic nanoparticles. Preliminary studies have demonstrated that iron oxide particles modified with cerium elements exhibit physicochemical properties unparalleled by unaltered iron oxides, such as an enhanced electrochemical buffering capacity and an abundance of hydroxyl radicals on the nanoparticle surface [19–22]. This is attributed to cerium's unique 4f electron shell structure, which upon doping effectively alters the bandgap of α-Fe_2O_3, thereby modifying its physicochemical characteristics [23,24]. Incorporating these modified iron oxide particles into water-based coatings as a crucial component is expected to markedly enhance the coating's corrosion resistance and self-healing capabilities, offering a novel technological pathway for the expansion of iron oxide coating applications. Wu et al. [25] found that the precursor concentration (reaction concentration) is crucial for the morphology, size, and physicochemical properties of nanomicelles. At lower precursor concentrations, the ionic concentration and polymer groups are prone to form stable complexes, which in turn enables the controlled growth of modified nanoparticles and alters the surface chemical properties of the nanoparticles. In addition to the different mechanisms of action of modifying elements on the physicochemical properties of the nanoparticles, the ionic concentration in the precursor solution also plays a role in the properties of the composite nanoparticles. In summary, this study successfully synthesized cerium-modified nanocrystalline iron oxide particles via a hydrothermal method and examined the effects of varying $c(Ce^{4+}):c(Fe^{3+})$ ratios in the precursor on the crystal structure, bandgap characteristics, and acid-base buffering capacity of the modified iron oxide. Concurrently, different cerium-modified iron oxide nanoparticles were formulated into aqueous coatings to assess their corrosion resistance and self-healing capabilities. The findings not only led to the development of a high-performance modified iron-oxide coating material with exceptional corrosion resistance but also elucidated to some extent the mechanisms by which cerium modifies iron oxide. Furthermore, we analyzed both the corrosion resistance mechanisms and self-healing properties of these coatings. This research aims to explore strategies to improve the protective effect of iron oxide coatings in corrosive media and investigate the possibility of optimization through chemical modification. By comparing various formulations of iron oxide coatings regarding their corrosion resistance performance, this study seeks to provide the theoretical basis and technical support for the development of new high-performance iron oxide coating materials.

2. Experimental

2.1. Raw Materials

The raw materials used for the preparation of the Ce-doped iron oxide particles in this study were Cerium sulfate($Ce(SO_4)_2$), iron sulfate($Fe_2(SO_4)_3$), sodium hydroxide(NaOH), sulfuric acid(H_2SO_4), and anhydrous ethanol (AR; Sino-Pharm Chemical Reagent Co., Ltd., Shanghai, China). The raw materials for the preparation of the waterborne iron oxide coatings mainly included acrylic resin, dispersant, defoamer, glycol, and thickener, all of which were purchased from Sino-Pharm Chemical Reagent Co., Ltd. The NaCl used to perform the corrosion resistance experiments was purchased as an analytically pure reagent from Sino-Pharm Chemical Reagent Co., Ltd. A commercially available iron oxide

nanoparticle with high electrochemical stability from Bayer Company (Shanghai, China) was chosen as a comparison sample.

2.2. Preparation of Ce-Doped Iron Oxide Particles

Ce-doped iron oxides were synthesized by the hydrothermal method under different $c(Ce^{4+})$:/$c(Fe^{3+})$ conditions. $Ce(SO_4)_2$ and $Fe_2(SO_4)_3$ were completely dissolved in distilled water. Then, the mass of $Fe_2(SO_4)_3$ was fixed, and the mass of $Ce(SO_4)_2$ was adjusted to the $c(Ce^{4+})$:$c(Fe^{3+})$ ratios of 1:40, 1:60, and 1:100, respectively, and the pH values of the three mixtures were adjusted with the NaOH solution. After thorough stirring, the mixtures were weighed and placed in a titanium autoclave. The autoclave temperature was set and maintained for a certain period of time, and stirring was maintained at a constant speed during the hydrothermal reaction. The hydrothermal reaction product was then cooled to room temperature naturally, and the final solid product was collected by centrifugation and washed with plenty of distilled water and ethanol to remove all impurities. Nano-iron oxide produced by Bayer was selected as the comparison sample. All process parameters are listed in Table 1.

Table 1. Process parameters.

Element	Parametric
Indoor temperature	25 °C
Initial volume of precursor	600 mL
Concentration of NaOH solution	2 M
Final pH of the precursor	8
Stirring time of precursors	30 min
Volume of precursor in reactor	250 mL
Holding time	1 h
Holding temperature	160 °C
Mixing speed	200 rpm

2.3. Preparation of Nano-Ferric Oxide Water-Based Acrylic Coatings

In this study, four different nanosized iron oxide were dispersed evenly in aqueous acrylic resins using a high-speed disperser (FS-1100D, Hangzhou, China). Before the addition of acrylic resin and thickener, the nanometer iron oxide particles were initially mixed with all additives at 1200 rpm for 30 minutes. Then, acrylic resin and thickener were slowly added and fully mixed at a low speed of 300 rpm to ensure that the mixture maintained a stable emulsification. The specific composition of the nanometer iron oxide water-based acrylic coating is shown in Table 2. Q235 carbon steel (C: 0.17–0.24%; Si: 0.17–0.37%; Mn: 0.35–0.65%; S: >0.030%; P: >0.030%) was used as a square metal substrate, with a diameter of 10 mm × 10 mm and a thickness of 2 mm. The surface of the substrate was sanded with 360#, 600#, 1000#, and 1500# sandpaper, followed by a thorough cleaning with anhydrous ethanol and acetone. The coating was uniformly sprayed with a high-pressure spray gun (IWATAW-71) at 25 °C until the average dry thickness of the coating reached 50 ± 5 μm. The coating thickness was measured using a digital laser-thickness gauge (QNIX4200, QNix, Cologne, Germany). After completing the above steps, the coating was dried in an oven at 60 °C for two consecutive days.

Table 2. Raw materials for the preparation of waterborne coatings.

Additive	wt/%
Acrylic Resins	33.0
Dispersants	0.2
Defoamers	0.2
Glycol	0.8
Iron oxide pigments	35.0
Distilled water	29.0

Table 2. *Cont.*

Additive	wt/%
Thickening agent	1.0
Others	0.8

2.4. Preparation of Electrodes

Characterization

X-Ray diffraction (XRD) (PANalytical, X'pert PRO, Almelo, the Netherlands) with Cu K_α (λ = 1.5418 Å) was used for phase analysis of nanoparticles. The scanning step length was 2° per minute, and the scanning range was 20° to 70°. According to Scheler's formula, the crystal size of the nanoparticles was calculated by using the crystal structure analysis software Jade6 (Materials Data Inc., Livermore, CA, USA) [26–28]:

$$D = \frac{K\lambda}{\beta \cos\theta} \quad (1)$$

where D is the average grain size (nm), K is the coefficient (use K = 0.9), λ is the $K\alpha$ X-Ray wavelength with Cu target (1.5418 Å), β is the broadening of the peak at its half maximum (FWHM), and θ is the half diffraction of the peaks.

Low-resolution and high-resolution images of the nanoparticles were detected using a transmission electron microscope (TEM) (JEOL, JEM 2100, Tokyo, Japan) at an accelerated voltage of 200 kV. The microscopic morphology of the coating was obtained by scanning electron microscopy (SEM) (Zeiss, ULTRA PLU, Oberkochen, Germany). Fourier transform infrared (FTIR) spectroscopy (Thermo Nicolet, NicolET-380, Minneapolis, MN, USA) was used to study the bonding modes of the sample in the range of 4000–400 cm^{-1}. The electrochemical properties of the coatings were measured using the Autolab electrochemical workstation (Metrohm, Autolab, Utrecht, Switzerland). The scanning rate was 3 mVs^{-1}, and the scanning potential ranged from −0.5 to +1 V (vs. OCP). The electrochemical detection was carried out at room temperature in a 3.5 wt% sodium chloride solution. The electrochemical results were analyzed by the NOVA 1.10 software provided by the Autolab electrochemical workstation. The coating-brine corrosion test was carried out according to the national standard "GB/T 10,834-2008" [29] of the People's Republic of China. The surface of the coating was treated by the "cross method", soaked in 3.5 wt% NaCl solution for 24 h, and then washed and dried; the surface corrosion was observed by SEM.

3. Result and Discussion

Figure 1 shows that the Ce-doped iron oxide samples prepared under different $c(Ce^{4+})$:$c(Fe^{3+})$ conditions detected the characteristic peak of α-Fe_2O_3 (JCPDS 33-0664), and all have a hexagonal structure. In the sample prepared under the condition of $c(Ce^{4+})$:$c(Fe^{3+})$ = 1:10, the broadening phenomenon of CeO_2 (JCPDS 34-0394) (111) characteristic peak is detected, which is due to the CeO_2 nanoparticles on the surface of α-Fe_2O_3, and the dispersion phenomenon may occur on the sample surface during detection [30]. The average grain size and lattice constant of Ce-doped α-Fe_2O_3 under different $c(Ce^{4+})$:$c(Fe^{3+})$ conditions can be obtained by calculating Figure 1 with the Jade 6.0 analysis software, as shown in Table 3. It can be seen from the table that with the gradual decrease in $c(Ce^{4+})$:$c(Fe^{3+})$, the lattice constant of the sample gradually increases. However, when $c(Ce^{4+})$:$c(Fe^{3+})$ = 1:100, the lattice constant of the sample decreases sharply. It is concluded that when the concentration of cerium in the solution is high, some Ce elements enter the α-Fe_2O_3 lattice to cause lattice distortion, but excessive $c(Ce^{4+})$:$c(Fe^{3+})$ inhibits lattice distortion. With the gradual decrease in $c(Ce^{4+})$:$c(Fe^{3+})$, the degree of the lattice disturbance of the sample increases gradually, and the average particle size increases gradually. When $c(Ce^{4+})$:$c(Fe^{3+})$ = 1:100, the low concentration of cerium is also not conducive to the lattice distortion of α-Fe_2O_3.

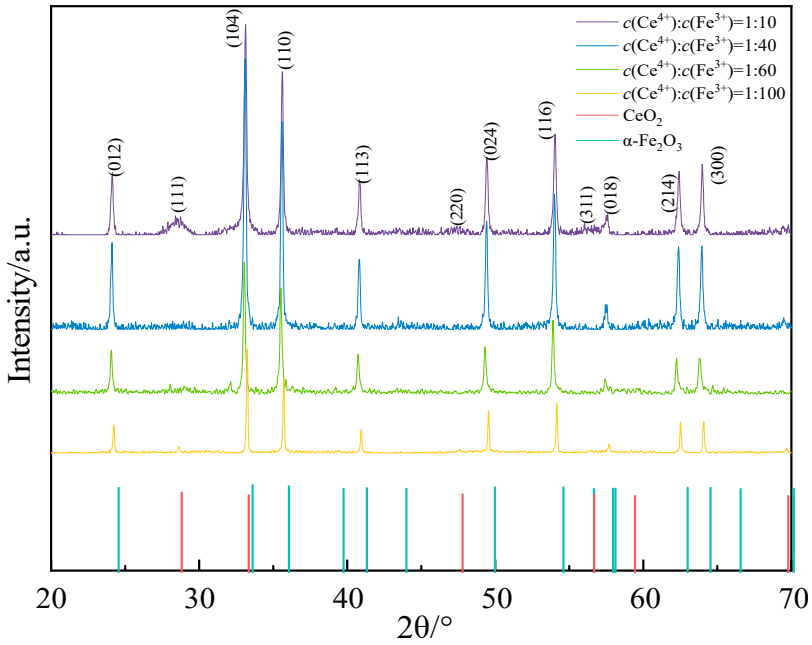

Figure 1. XRD patterns of Ce-doped iron oxide samples.

Table 3. Average grain size and lattice constant of the nanoparticles.

Samples	Average Grain Size/nm	Lattice Constant/a,b	Lattice Constant/c
$c(Ce^{4+}):c(Fe^{3+})$ = 1:10 [1]	99.8	0.5036	1.3758
$c(Ce^{4+}):c(Fe^{3+})$ = 1:40 [1]	117.4	0.5039	1.3763
$c(Ce^{4+}):c(Fe^{3+})$ = 1:60 [1]	126.9	0.5047	1.3794
$c(Ce^{4+}):c(Fe^{3+})$ = 1:100 [1]	151.6	0.5029	1.3717
CeO_2 [2]	-	0.5387	0.5387
Bayer α-Fe_2O_3	77.0	0.5014	1.3713

[1] Ce-doped iron oxide and [2] CeO_2 nanoparticles.

Ce-doped iron oxide nanoparticles under different $c(Ce^{4+}):c(Fe^{3+})$ conditions are further characterized by TEM mapping. As shown in Figure 2d, in the sample with a $c(Ce^{4+}):c(Fe^{3+})$ ratio of 1:100, cerium elements are mainly distributed on the surface of Ce-doped iron oxide nanoparticles. As shown in Figure 2a–c, with the gradual increase in $c(Ce^{4+}):c(Fe^{3+})$, the cerium gradually diffuses into the interior of the Ce-doped α-Fe_2O_3 particles. Although it is difficult for cerium to form in lattice doping under the condition of solution pH = 8 [31], the doping of cerium ions into the interior of the iron oxide lattice occurs when the concentration of cerium in a solution is high.

Figure 3 shows the HRTEM and SAED results of the Ce-doped iron oxide samples under different $c(Ce^{4+}):c(Fe^{3+})$ conditions. It can be seen from the results that the CeO_2 crystal face appears on the surface of the Ce-doped iron oxide particles prepared under different $c(Ce^{4+}):c(Fe^{3+})$ conditions and preferentially grows along the crystal face (111). In Figure 3a,b, in the Ce-doped iron oxide particles prepared under the conditions of $c(Ce^{4+}):c(Fe^{3+})$ = 1:10 and 1:40, the crystal surface spacing of the CeO_2 [32–34] does not change significantly, indicating that there is no lattice distortion. As shown in Figure 3c,d, the spacing of the CeO_2 crystal faces decrease in the Ce-doped α-Fe_2O_3 prepared under the conditions of $c(Ce^{4+}):c(Fe^{3+})$ = 1:60 and 1:100, and the spacing of the CeO_2 crystal faces decrease to a greater extent when $c(Ce^{4+}):c(Fe^{3+})$ = 1:60. It shows that with the decrease in $c(Ce^{4+}):c(Fe^{3+})$, some Fe^{3+} ions may be reverse-doped and enter the interior of the CeO_2 lattice. According to the doping theory [35], when elements with small ionic radii are doped into molecules with large ionic radii, the crystal plane's spacing will be reduced. The crystal-surface spacing of α-Fe_2O_3 in Ce-doped α-Fe_2O_3 prepared under different

$c(Ce^{4+})$:$c(Fe^{3+})$ conditions increases, indicating that CeO_2 is not only adsorbed on the surface of α-Fe_2O_3 particles, but also that the Ce element can enter the inside of iron oxide and cause lattice distortion.

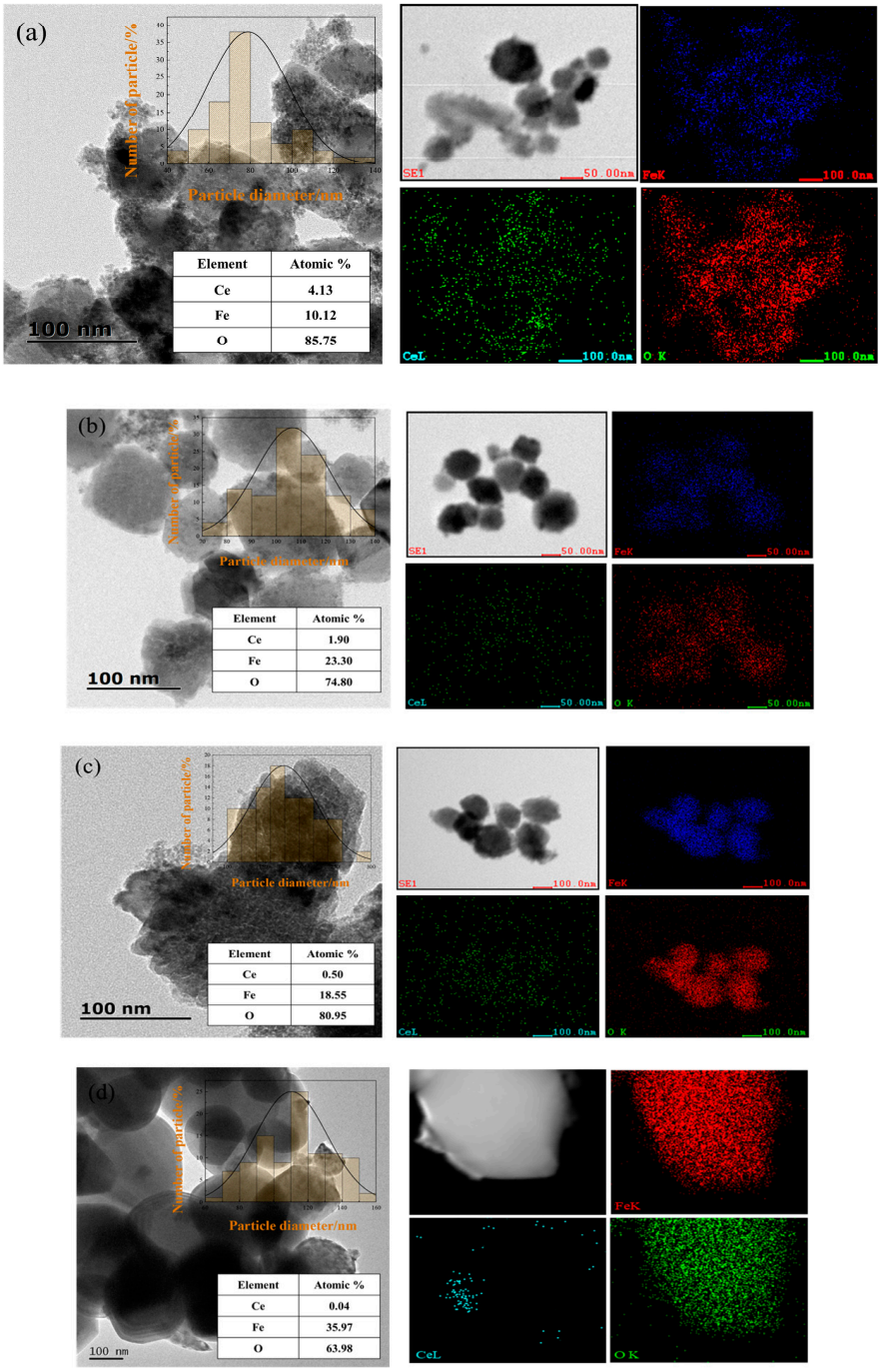

Figure 2. TEM and mapping images of the samples: (**a**) $c(Ce^{4+})$:$c(Fe^{3+})$ = 1:10, (**b**) $c(Ce^{4+})$:$c(Fe^{3+})$ = 1:40, (**c**) $c(Ce^{4+})$:$c(Fe^{3+})$ = 1:60, and (**d**) $c(Ce^{4+})$:$c(Fe^{3+})$ = 1:100.

Figure 4a shows a wide-band Fourier transform infrared spectrum at room temperature. It depicts the infrared absorption peaks of cerium oxide at 3455 cm^{-1}, 2357 cm^{-1}, 1635 cm^{-1}, 1385 cm^{-1}, 1045 cm^{-1}, and 555 cm^{-1} [36]. The absorption bands at 3455 cm^{-1}, 1385 cm^{-1}, and 1045 cm^{-1} represent the tensile and flexural vibrations of cerium oxide on water, respectively. At 2357 cm^{-1}, absorption spectra were observed due to the absorption of CO_2 by nanoparticles. The peaks at 1635 cm^{-1} and 555 cm^{-1} belong to the asymmetric stretching and symmetric vibration bands of Ce-O, respectively. The crystal structures of

four samples under different $c(Ce^{4+}):c(Fe^{3+})$ conditions were studied by means of atomic and molecular vibration, and the FITR pattern of the Fe-O bond in Figure 4a was magnified to obtain the fine spectrum in Figure 4b. Fe-O stretching vibration peaks were detected at 569 cm^{-1}, 566 cm^{-1}, 563 cm^{-1}, and 567 cm^{-1} of the four Ce-doped α-Fe_2O_3 particles in Figure 4b. The blue shift of Fe-O bonds is the largest when $c(Ce^{4+}):c(Fe^{3+})$ = 1:10, and the smallest when $c(Ce^{4+}):c(Fe^{3+})$ = 1:60. It shows that the Fe-O bond energy of the sample is higher and the carrier binding ability is stronger at the higher $c(Ce^{4+}):c(Fe^{3+})$ condition, while the carrier binding ability of the sample is weaker at the lower $c(Ce^{4+}):c(Fe^{3+})$ condition. Ce-ion doping results in the expansion of the α-Fe_2O_3 lattice and the shortening of the Fe-O bond length. From the formula of molecular vibration frequency [37], it can be seen that cerium doping can improve the ferrite bond's energy and stability. In past studies, this phenomenon has been analyzed in detail, mainly based on the quantum scale effect of nanoparticles [17,18,20].

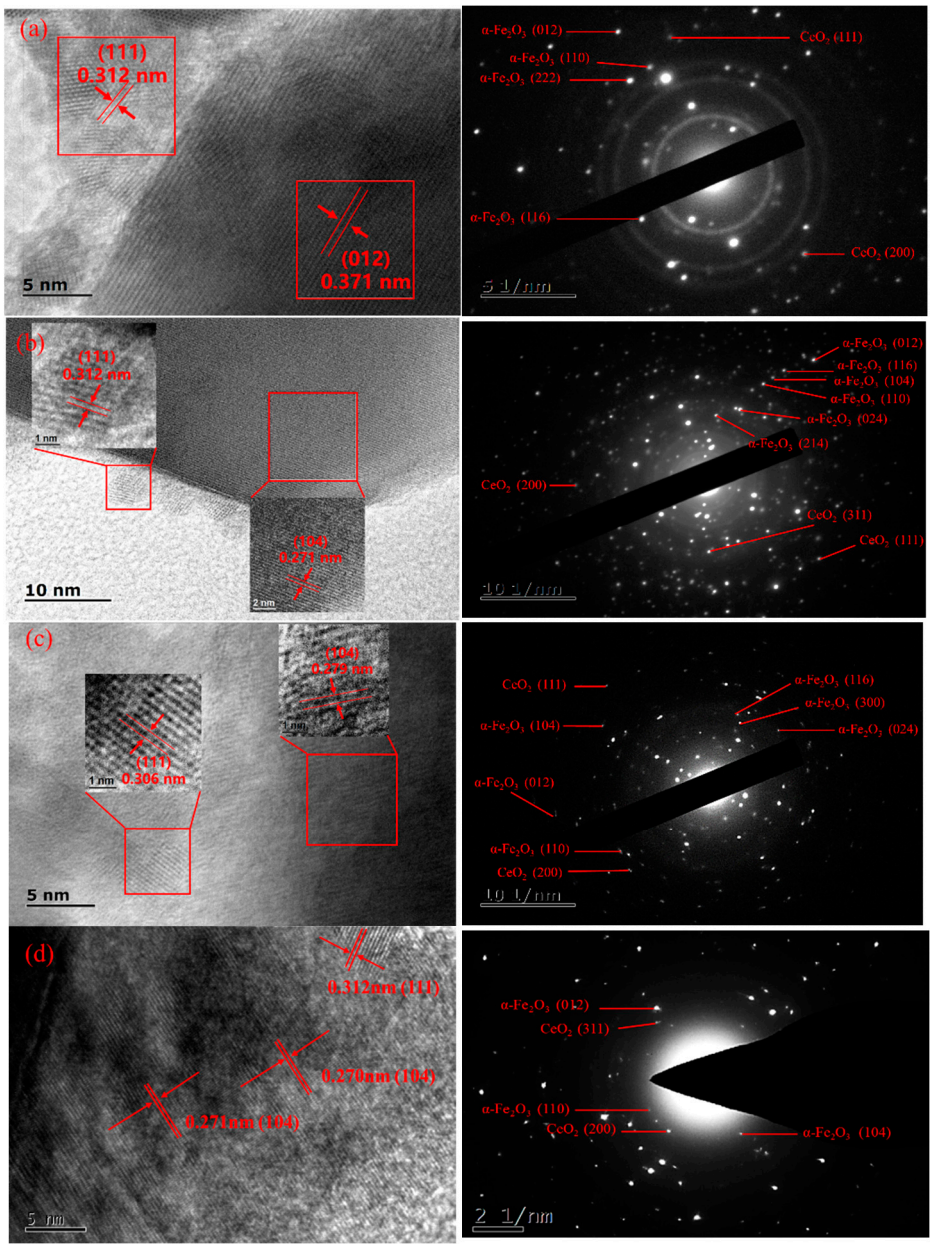

Figure 3. High resolution image and diffraction spots of samples: (**a**) $c(Ce^{4+}):c(Fe^{3+})$ = 1:10, (**b**) $c(Ce^{4+}):c(Fe^{3+})$ = 1:40, (**c**) $c(Ce^{4+}):c(Fe^{3+})$ = 1:60, and (**d**) $c(Ce^{4+}):c(Fe^{3+})$ = 1:100.

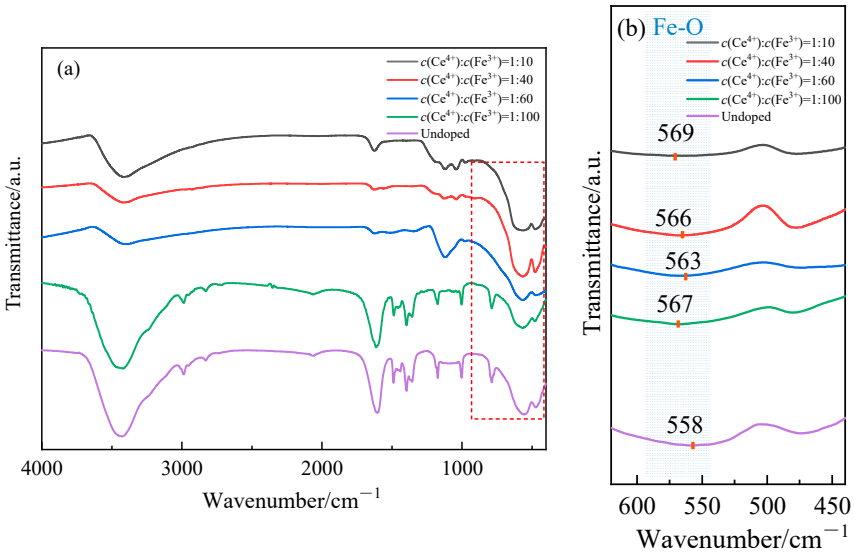

Figure 4. FTIR (Fourier transform infrared) spectrum of samples. (**a**) Wide range FTIR spectrum; (**b**) Narrow range FTIR spectrum.

The characterization of various Ce-doped iron oxide nanoparticles under different $c(Ce^{4+}):c(Fe^{3+})$ conditions is shown in Figure 5. The crystal structure formation mechanism of the Ce-doped α-Fe_2O_3 nanoparticles under different pH conditions has been proposed in previous studies. When pH = 8, Ce ions will not form the lattice doping of α-Fse Cee_2O_3, because O_2 can only adhere to the surface of α-Fe_2O_3 particles due to the influence of heterogeneous nucleation [38,39]. The crystal structure of Ce-doped α-Fe_2O_3 prepared under the condition of $c(Ce^{4+}):c(Fe^{3+})$ = 1:100 is the same as that of the Ce-doped α-Fe_2O_3 prepared in this study. With the increase in $c(Ce^{4+}):c(Fe^{3+})$, when $c(Ce^{4+}):c(Fe^{3+})$ = 1:60, Fe^{3+} ions are doped into the inside of the CeO_2 lattice, forming the lattice distortion of CeO_2 crystal. When the $c(Ce^{4+}):c(Fe^{3+})$ is 1:10, the formation of Fe-doped CeO_2 crystals is obviously hindered by excessive CeO_2 nanoparticles. Therefore, a too large or too small ratio of cerium ions (Ce^{4+}) to iron ions (Fe^{3+}) is not conducive to the formation of a Fe-doped CeO_2 crystal structure. When the $c(Ce^{4+}):c(Fe^{3+})$ = 1:60, Ce-doped α-Fe_2O_3 and Fe-doped CeO_2 heterostructures are most easily formed.

Figure 6 shows the potentiodynamic polarization curves of undoped iron oxide, Bayer iron oxide, and Ce-doped iron oxide under different $c(Ce^{4+}):c(Fe^{3+})$ conditions. The corrosion potential (E_c), corrosion current (I_c), and breakdown potential (E_b) of the sample are obtained from Figure 6 and are listed in Table 4. As the ratio of $c(Ce^{4+}):c(Fe^{3+})$ increases, the corrosion potential initially decreases and then rises, while the corrosion current density gradually decreases. When the ratio of $c(Ce^{4+}):c(Fe^{3+})$ = 1: 60, the electrochemical stability of Ce-doped α-Fe_2O_3 has an inflection point, indicating that the modified iron oxide under this condition had the lowest corrosion potential (−420.41 mV) due to its low Fe-O bond energy and poor electrochemical stability. It can be seen that the slope of the anodic curve of Ce-doped α- Fe_2O_3 under the condition of $c(Ce^{4+}):c(Fe^{3+})$ = 1: 60 is larger, which indicates that it has a strong inhibition of anodic polarization, although its electrochemical stability is weaker, which may be related to its tendency to produce dense corrosion products that impede the anodic reaction in corrosive media. The slopes of the cathodic polarization curves of the samples were all the same, indicating that the inhibition of ion migration ability of several coating samples is the same. When the ratio of $c(Ce^{4+}):c(Fe^{3+})$ exceeds 1: 60, the corrosion current is significantly higher than that of commercial Bayer iron oxide and undoped iron oxide, indicating that the Ce-doped iron oxide exhibits greater electrochemical stability than the commercial Bayer nanoscale iron oxide.

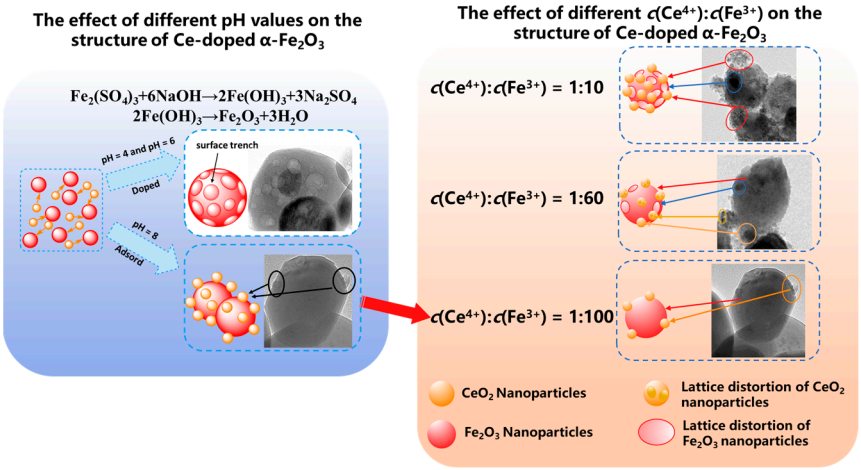

Figure 5. Schematic diagram of the formation mechanism of Ce-doped iron oxide under different $c(Ce^{4+}):c(Fe^{3+})$ conditions.

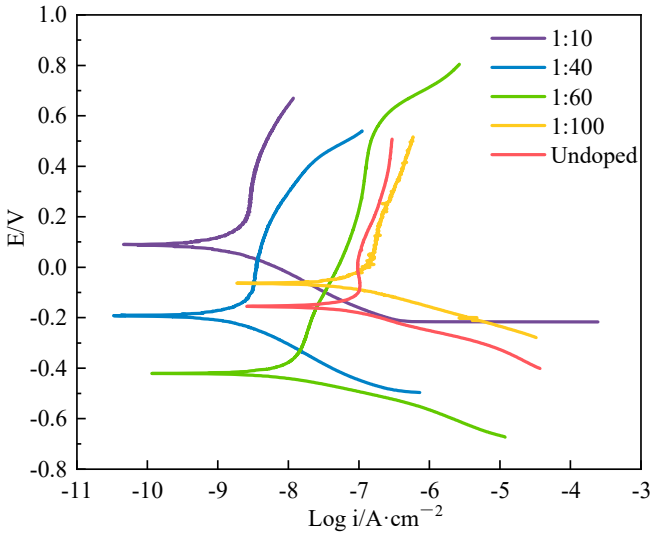

Figure 6. Electrochemical test of the samples.

Table 4. Electrochemical test results of the samples.

Sample	E_c/mV	I_c/μA·cm^{-2}	E_b/mV
$c(Ce^{4+}):c(Fe^{3+})$ = 1:10	89.63	0.002	400.87
$c(Ce^{4+}):c(Fe^{3+})$ = 1:40	−192.72	0.003	211.63
$c(Ce^{4+}):c(Fe^{3+})$ = 1:60	−420.41	0.011	570.17
$c(Ce^{4+}):c(Fe^{3+})$ = 1:100	−64.21	0.143	166.18
Undoped α-Fe_2O_3	−155.12	0.116	29.37
Bayer α-Fe_2O_3	−46.46	0.030	-

The Ce-doped α-Fe_2O_3 prepared under different $c(Ce^{4+}):c(Fe^{3+})$ conditions was prepared in a water-based acrylic coating. After soaking in a 3.5% NaCl solution for 24 h, the morphology and phase of the corrosion products at the scratch were observed. Figure 7 shows the SEM-EDS results of the coated samples after immersion. It can be seen from the figure that under the conditions of $c(Ce^{4+}):c(Fe^{3+})$ = 1:10 and 1:40, a large number of corrosion products are distributed on the coating surface, the coating/substrate interface and the substrate surface have fewer corrosion products, there are cracks on the surface, and the ratio of Fe:O atoms in the corrosion products ranges from 0.5 to 0.54. Under the conditions of $c(Ce^{4+}):c(Fe^{3+})$ = 1:60 and 1:100, the corrosion products are mainly distributed

in the scratches, the corrosion product film is still relatively dense, and the atomic ratio of Fe:O in the corrosion products ranges from 0.22 to 0.25.

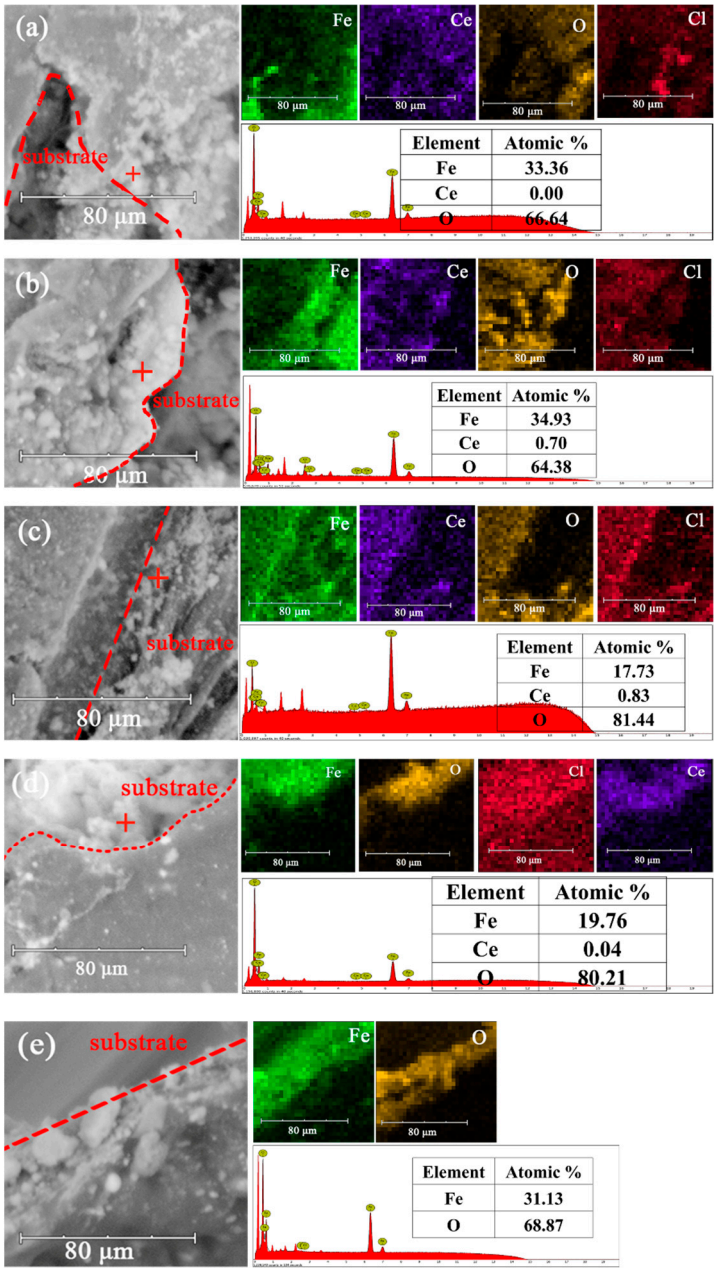

Figure 7. SEM-EDS results of the coatings immersed in the NaCl solution: (**a**) $c(Ce^{4+}):c(Fe^{3+})$ = 1:10, (**b**) $c(Ce^{4+}):c(Fe^{3+})$ = 1:40, (**c**) $c(Ce^{4+}):c(Fe^{3+})$ = 1:60, (**d**) $c(Ce^{4+}):c(Fe^{3+})$ = 1:100, and (**e**) undoped.

Figure 8 shows the XRD results of the corrosion products of the four coatings at the scratch. It can be seen from the figure that the main phase of the corrosion product film in the coatings with $c(Ce^{4+}):c(Fe^{3+})$ = 1:10 and 1:40 is α-Fe_2O_3 (JCPDS 33-0664). In $c(Ce^{4+}):c(Fe^{3+})$ = 1:60 and 1:100, the main phase of the corrosion product film is α-FeOOH (JCPDS 29-0713). According to the literature [40–43], when α-Fe_2O_3 is the main phase in the corrosion product film, the morphology is loose and porous, and the shielding effect on the corrosive particles is weak. When α-FeOOH is the main phase in the corrosion product film, the density is much higher than α-Fe_2O_3, and α-FeOOH has stronger physical shielding ability for the corrosive particles. Therefore, under the conditions of this experiment, the Ce-doped α-Fe_2O_3 prepared by a $c(Ce^{4+}):c(Fe^{3+})$ ratio of 1:60 has a certain self-healing ability because it is easy to produce α-FeOOH in the electrolyte solution.

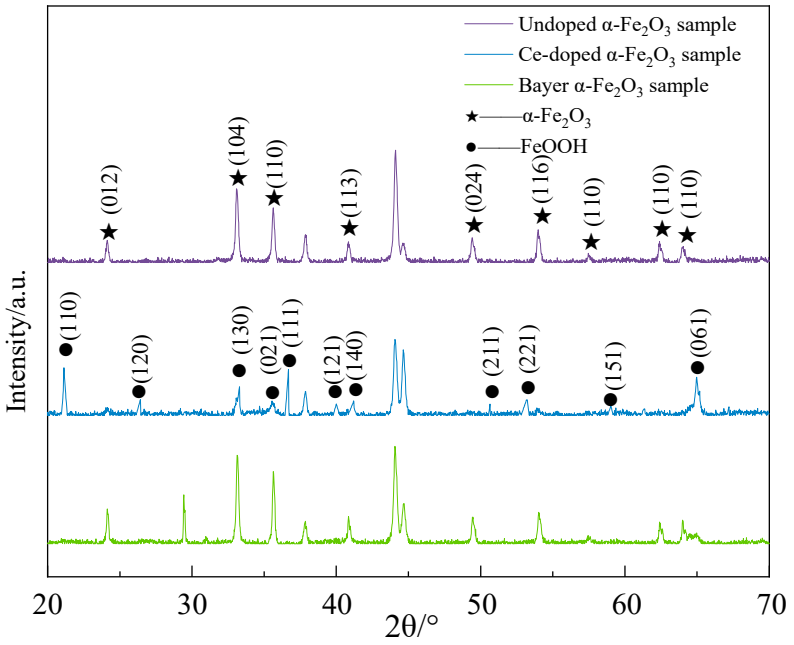

Figure 8. XRD patterns of the coatings after immersion in a 3.5% NaCl solution for 24 h.

4. Conclusions

This research involved the synthesis of Ce-doped α-Fe_2O_3 nanoparticles using the hydrothermal method with different molar ratios of Ce^{4+} to Fe^{3+} and their applications in the production of water-based acrylic coatings. The experimental results show that the coating exhibits the best corrosion resistance and self-healing ability when the $c(Ce^{4+}):c(Fe^{3+})$ = 1:60. XRD, TEM, and HRTEM studies demonstrated the impact of doping on the crystal structure and lattice parameter of α-Fe_2O_3, while FTIR spectra analysis demonstrated that the presence of Ce inα-Fe_2O_3 resulted in an increase in the bond energy and stability of Fe-O bonds. The results of the electrochemical test provide additional evidence supporting the increased electrochemical stability of Ce-doped α-Fe_2O_3 when the ratio of $c(Ce^{4+}):c(Fe^{3+})$ is 1:60. Additionally, the SEM-EDS and XRD analyses indicate that the corrosion product of the coating in a 3.5% NaCl solution under the condition of $c(Ce^{4+}):c(Fe^{3+})$ = 1:60 consists mainly of α-FeOOH, with a density superior to that ofα-Fe_2O_3. This suggests that the coating possesses enhanced physical shielding capabilities. These results offer theoretical and technical backing for the creation and advancement of novel high-efficiency coating materials and hold significant importance for the utilization of nanotechnology in anticorrosion coating applications and related industry growth.

Author Contributions: J.N.: Conceptualization, data curation, formal analysis, methodology, funding acquisition, project administration, writing—original draft, writing—review and editing; J.N. and X.T.: methodology, data curation, validation, writing—review and editing; P.S.: project administration, project administration. All authors have read and agreed to the published version of the manuscript.

Funding: This research was funded by the Planning Projects of the Liaoning Provincial Association for Non-Government Education of China (Grant No. LMJX2023173), the Pilot Projects of Liaoning Zhonghua Vocational Education Society of China (Grant No. XTZ2024029), and the Dalian Art College (Grant No. ZX2023002).

Data Availability Statement: The data that support the findings of this study are available from the corresponding author, Junxiang Ning, upon reasonable request.

Conflicts of Interest: The authors declare no conflicts of interest.

References

1. Kang, D.; Lee, M.; Lee, S.J.; Kim, J.; Ryu, G.H. Enhanced adhesion and corrosion resistance of reduced graphene oxide coated-steel with iron oxide nanoparticles. *Appl. Surf. Sci.* **2023**, *624*, 157121. [CrossRef]
2. Agustín-Sáenz, C.; Santa Coloma, P.; Fernández-Carretero, F.J.; Brusciotti, F.; Brizuela, M. Design of corrosion protective and antistatic hybrid sol-gel coatings on 6xxx almgsi alloys for aerospace application. *Coatings* **2020**, *10*, 441. [CrossRef]
3. Krishna, L.R.; Madhavi, Y.; Babu, P.S.; Rao, D.S.; Padmanabham, G. Strategies for corrosion protection of non-ferrous metals and alloys through surface engineering. *Mater. Today Proc.* **2019**, *15*, 145–154. [CrossRef]
4. Liu, T.; Liu, Y.; Ye, Y.; Li, J.; Yang, F.; Zhao, H.; Wang, L. Corrosion protective properties of epoxy coating containing tetraaniline modified nano-α-Fe2O3. Prog. *Org. Coat.* **2019**, *132*, 455–467. [CrossRef]
5. Li, J.; Meng, F.; Liu, L.; Cui, Y.; Liu, R.; Zheng, H.; Wang, F. Effect of nano-α-Fe2O3/graphene oxide hybrids on the corrosion resistance of epoxy coating under alternating hydrostatic pressure. *Corros. Commun.* **2022**, *5*, 62–72. [CrossRef]
6. Hu, J.; He, S.; Wang, Z.; Zhu, J.; Wei, L.; Chen, Z. Stearic acid-coated superhydrophobic Fe2O3/Fe3O4 composite film on n80 steel for corrosion protection. *Surf. Coat. Technol.* **2019**, *359*, 47–54. [CrossRef]
7. Dorado, F.; Toledo, L.; de la Osa, A.R.; Esteban-Arranz, A.; Sacristan, J.; Pellegrin, B.; Steck, J.; Sanchez-Silva, L. Adhesion enhancement and protection of concrete against aggressive environment using graphite-Fe_2O_3 modified epoxy coating. *Constr. Build. Mater.* **2023**, *379*, 131179. [CrossRef]
8. Fan, W.; Wang, H.; Wang, C.; Liu, Z.; Wang, Z.; Liu, S.; Zhu, Y. Oxygen vacancy modified α-Fe_2O_3 nanorods provide an environment-friendly and efficient anti-corrosion passive film into polymer coating. *Corros. Sci.* **2023**, *215*, 111045. [CrossRef]
9. Sumi, V.S.; Arunima, S.R.; Deepa, M.J.; Sha, M.A.; Riyas, A.H.; Meera, M.S.; Saji, V.S.; Shibli, S. Pani- Fe_2O_3 composite for enhancement of active life of alkyd resin coating for corrosion protection of steel. *Mater. Chem. Phys.* **2020**, *247*, 122881. [CrossRef]
10. Chen, Y.; Wen, S.; Wang, J.; Wang, G.; Wang, C.; Wang, Y.; Li, S.; Zhang, J. Preparation of α-Fe_2O_3@ TA@ GO composite material and its anticorrosion performance in epoxy modified acrylic resin coatings. *Prog. Org. Coat.* **2021**, *154*, 105987. [CrossRef]
11. Grundmeier, G.; Schmidt, W.; Stratmann, M. Corrosion protection by organic coatings: Electrochemical mechanism and novel methods of investigation. *Electrochim. Acta* **2000**, *45*, 2515–2533. [CrossRef]
12. Tang, F.; Chen, G.; Brow, R.K.; Volz, J.S.; Koenigstein, M.L. Corrosion resistance and mechanism of steel rebar coated with three types of enamel. *Corros. Sci.* **2012**, *59*, 157–168. [CrossRef]
13. Popoola, A.; Olorunniwo, O.E.; Ige, O.O. Corrosion resistance through the application of anti-corrosion coatings. *Dev. Corros. Prot.* **2014**, *13*, 241–270.
14. Han, X.; Ren, L.; Ma, Y.; Gong, X.; Wang, H. A mussel-inspired self-repairing superhydrophobic coating with good anti-corrosion and photothermal properties. *Carbon.* **2022**, *197*, 27–39. [CrossRef]
15. Herrmann, S.; Kostrzewa, M.; Wierschem, A.; Streb, C. Polyoxometalate ionic liquids as self-repairing acid-resistant corrosion protection. *Angew. Chem. Int. Ed.* **2014**, *53*, 13596–13599. [CrossRef]
16. Shchukin, D.G.; Möhwald, H. Self-repairing coatings containing active nanoreservoirs. *Small* **2007**, *3*, 926–943. [CrossRef]
17. Takami, S.; Sato, T.; Mousavand, T. Hydrothermal synthesis of surface-modified iron oxide nanoparticles. *Mater. Lett.* **2007**, *61*, 4769–4772. [CrossRef]
18. Bagheri, S.; Julkapli, N.M. Modified iron oxide nanomaterials: Functionalization and application. *J. Magn. Magn. Mater.* **2016**, *416*, 117–133. [CrossRef]
19. Ning, J.; Shi, P.; Jiang, M.; Liu, C.; Jia, Z. Ce-doped α- Fe2O3 nanoparticles prepared by hydrothermal method used in corrosion-resistant field: Effects of ph on the structure, morphology and chemical stability. *Appl. Phys. A* **2021**, *127*, 604. [CrossRef]
20. Ning, J.; Shi, P.; Jiang, M.; Liu, C.; Li, X. Effect of ce doping on the structure and chemical stability of nano-α- Fe2O3. *Nanomaterials* **2019**, *9*, 1039. [CrossRef]
21. Ning, J.; Shi, P.; Jiang, M.; Liu, C.; Jia, Z. Synthesis and characterization of cerium oxide/iron oxide nanocomposite and its surface acid-base characteristics. *J. Environ. Chem. Eng.* **2021**, *9*, 105540. [CrossRef]
22. Wang, H.; Shi, P.; Ning, J. Synthesis, characterization, and electrochemical properties of La-doped α- Fe_2O_3 nanoparticles. *Nanomaterials* **2022**, *12*, 3346. [CrossRef] [PubMed]
23. Herper, H.C.; Vekilova, O.Y.; Simak, S.I.; Di Marco, I.; Eriksson, O. Localized versus itinerant character of 4f-states in cerium oxides. *J. Phys. Condens. Matter* **2020**, *32*, 215502. [CrossRef] [PubMed]
24. Gangopadhyay, S.; Frolov, D.D.; Masunov, A.E.; Seal, S. Structure and properties of cerium oxides in bulk and nanoparticulate forms. *J. Alloy. Compd.* **2014**, *584*, 199–208. [CrossRef]
25. Wu, Z.; Ma, X.; Ma, Y. Core/Shell PEGS/HA hybrid nanoparticle via micelle-coordinated mineralization for tumor-specific therapy. *ACS Appl. Mater. Interfaces* **2020**, *12*, 12109–12119. [CrossRef] [PubMed]
26. Tamanna, N.J.; Hossain, M.S.; Bahadur, N.M.; Ahmed, S. Green synthesis of Ag_2O & facile synthesis of ZnO and characterization using ftir, bandgap energy & XRD (scherrer equation, williamson-hall, size-train plot, monshi-scherrer model). *Results Chem.* **2024**, *7*, 101313.
27. Miranda, M.; Sasaki, J.M. The limit of application of the scherrer equation. *Acta Crystallogr. Sect. A Found. Adv.* **2018**, *74*, 54–65. [CrossRef]
28. Muniz, F.T.L.; Miranda, M.R.; Morilla Dos Santos, C.; Sasaki, J.M. The scherrer equation and the dynamical theory of X-ray diffraction. *Acta Crystallogr. Sect. A: Found. Adv.* **2016**, *72*, 385–390. [CrossRef]

29. Chen, C.; Fang, L.; Zhang, R.; Jiu, S.; Song, Q.; Chen, Y. Zinc-rich inorganic silicate anticorrosive coating incorporating muscovite for steel bars in sand-based autoclaved aerated concrete. *J. Build. Eng.* **2024**, *82*, 108316. [CrossRef]
30. Bera, P.; Priolkar, K.R.; Gayen, A.; Sarode, P.R.; Hegde, M.S.; Emura, S.; Kumashiro, R.; Jayaram, V.; Subbanna, G.N. Ionic dispersion of pt over CeO_2 by the combustion method: Structural investigation by XRD, TEM, XPS, and EXAFS. *Chem. Mater.* **2003**, *15*, 2049–2060. [CrossRef]
31. Akbari, B.; Tavandashti, M.P.; Zandrahimi, M. Particle size characterization of nanoparticles-a practical approach. *Iran. J. Mater. Sci. Eng.* **2011**, *8*, 48–56.
32. Hailstone, R.K.; Difrancesco, A.G.; Leong, J.G.; Allston, T.D.; Reed, K.J. A study of lattice expansion in CeO_2 nanoparticles by transmission electron microscopy. *J. Phys. Chem. C* **2009**, *113*, 15155–15159. [CrossRef]
33. Zhang, H.; Gao, X.; Gong, B.; Shao, S.; Tu, C.; Pan, J.; Wang, Y.; Dai, Q.; Guo, Y.; Wang, X. Catalytic combustion of CVOCs over $MoOx/CeO_2$ catalysts. *Appl. Catal. B Environ.* **2022**, *310*, 121240. [CrossRef]
34. La, R.; Hu, Z.; Li, H.; Shang, X.; Yang, Y. Template synthesis of CeO2 ordered nanowire arrays. *Mater. Sci. Eng. A* **2004**, *368*, 145–148. [CrossRef]
35. Nakayama, M.; Martin, M. First-principles study on defect chemistry and migration of oxide ions in ceria doped with rare-earth cations. *Phys. Chem. Chem. Phys.* **2009**, *11*, 3241–3249. [CrossRef]
36. Fu, Y.; Lin, C.; Hsu, C. Preparation of ultrafine CeO_2 powders by microwave-induced combustion and precipitation. *J. Alloy. Compd.* **2005**, *391*, 110–114. [CrossRef]
37. Berthomieu, C.; Hienerwadel, R. Fourier transform infrared (FTIR) spectroscopy. *Photosynth. Res.* **2009**, *101*, 157–170. [CrossRef]
38. Gao, Y.; Wang, B.; Huang, J.; Gao, T.; Yang, W.; Xie, Q.; Chen, Q. Growth pattern of homogeneous and heterogeneous nucleation in high-entropy FeNiCrCoCu alloys. *Cryst. Growth Des.* **2022**, *22*, 2417–2425. [CrossRef]
39. Nammahachak, N.; Aup-Ngoen, K.K.; Asanithi, P.; Horpratum, M.; Chuangchote, S.; Ratanaphan, S.; Surareungchai, W. Hydrothermal synthesis of carbon quantum dots with size tunability via heterogeneous nucleation. *RSC Adv.* **2022**, *12*, 31729–31733. [CrossRef]
40. Jingxin Jian, Y.S.M.S. Cubic SiC photoanode coupling with Ni:FeOOH oxygen-evolution cocatalyst for sustainable photoelectrochemical water oxidation. *Sol. RRL* **2020**, *4*, 1900364. [CrossRef]
41. Fu, G.; Tang, X.; Liu, Q.; Su, Y.; Wang, X. Hot corrosion of Fe-Cr Alloys with 75 Na_2SO_4 + 25 NaCl coating at 1173 K. High Temp. *Mat. Pr.-Isr.* **2012**, *31*, 717–721.
42. Li, M.S.; Wang, L.; Zhang, S.J.; Luo, L.G. Oxidation-resistance of (Ti, Al, Nb) N Coatings Prepared by Arc Ion Plating. *Adv. Mater. Res.* **2014**, *941*, 1376–1379. [CrossRef]
43. Xu, B.; Wei, Z.; Hong, X.; Zhou, Y.; Gan, S.; Shen, M. Preparation and characterization of novel microencapsulated phase change materials with SiO_2/FeOOH as the shell for heat energy storage and photocatalysis. *J. Energy Storage* **2021**, *43*, 103251. [CrossRef]

Disclaimer/Publisher's Note: The statements, opinions and data contained in all publications are solely those of the individual author(s) and contributor(s) and not of MDPI and/or the editor(s). MDPI and/or the editor(s) disclaim responsibility for any injury to people or property resulting from any ideas, methods, instructions or products referred to in the content.